ACS APPLIED NANO MATERIALS

www.acsanm.org

Article

Synthesis of Pure and Fe-Doped TiO_2 Nanoparticles via Electrospray-Assisted Flame Spray Pyrolysis for Antimicrobial Applications

Jalal Poostforooshan,* Sabrina Belbekhouche,* Vinzent Olszok, Malte F. B. Stodt, Mira Simmler, Malte Bierwirth, Hermann Nirschl, Johannes Kiefer, Udo Fritsching, and Alfred P. Weber

Cite This: *ACS Appl. Nano Mater.* 2023, 6, 22660−22672

Read Online

ACCESS | Metrics & More | Article Recommendations | Supporting Information

ABSTRACT: We report a straightforward aerosol-based approach to synthesizing pure and Fe-doped TiO_2 nanoparticles by continuous electrospray-assisted flame spray pyrolysis (EAFSP). Initially, pure TiO_2 nanoparticles were prepared by electrospraying titanium diisopropoxide bis(acetylacetonate) (TDIP) at varying concentrations onto a grounded flame. In this regard, various *in situ* (phase Doppler anemometry, high-speed camera, and scanning mobility particle sizer) and *ex situ* (small-angle X-ray scattering, transmission electron microscopy, and BET adsorption isotherms) diagnostics were applied for the analysis of the in-flight droplet characteristics in the spray, such as droplet μ-explosions, as well as primary and agglomerate nanoparticle evolution within the process and the particulate product. Moreover, single-particle ICP-MS (inductively coupled plasma−mass spectrometry) *in situ* measurements have been conducted to get insight into the process that causes various particle morphologies and to open up the option of an *in situ* determination of the particle formation route. Subsequently, the EAFSP method was utilized to produce Fe-doped TiO_2 nanoparticles. The influences of the Fe^{3+} dopant concentration on the particle size, crystal structure, crystallite sizes, phase formation, oxygen vacancy defects, and optical gaps were systematically investigated. The presented EAFSP synthesis, in contrast to conventional flame spray pyrolysis (FSP) with gas atomization of the solvent/precursor, eliminates the need for dispersion gas and complex solvents, making it a more efficient and environmentally friendly method for nanoparticle synthesis. Finally, we studied the application potential of EAFSP-synthesized pure and Fe-doped TiO_2 nanoparticles for fighting bacteria resistant to an antibiotic, here spectinomycin-resistant *Escherichia coli*. A clear inhibitory effect of the Fe-doped TiO_2 nanoparticles could be observed during the growth of bacteria in the liquid medium, up to 99.4%. These results point out the high potential of the designed Fe-doped TiO_2 nanoparticles to act as antimicrobial agents and treatments against infections.

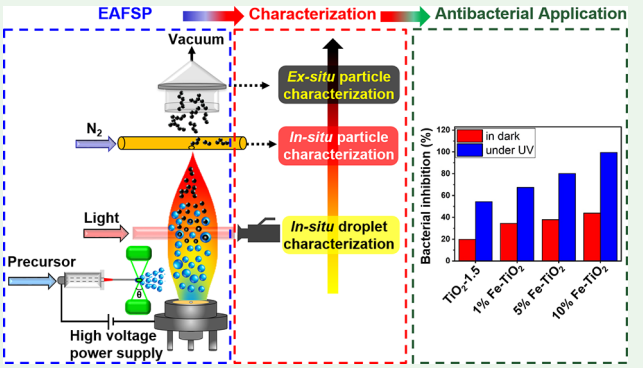

KEYWORDS: *electrospray-assisted flame spray pyrolysis, Fe-doped TiO_2 nanoparticles, bacteria resistant to antibiotic, spectinomycin-resistant bacteria, μ-explosions*

1. INTRODUCTION

TiO_2 is a semiconducting transition metal oxide with low cost, biocompatibility, and resistance to chemical erosion, making it a popular candidate in various fields such as solar cells[1] and photocatalysis.[2] Despite its numerous advantages, TiO_2 has some limitations, including its wide band gap energy, which limits its activity under visible light irradiation, and its relatively low photoquantum efficiency, which arises from the fast recombination of electron−hole pairs.[3] To address these limitations, researchers have investigated various strategies, including doping TiO_2 with transition metal ions, to enhance its photocatalytic properties.[4] Among the transition metal ions, iron has been found to be an effective dopant because the ionic radius of Fe^{3+} is similar to that of Ti^{4+}, allowing for easy incorporation into the TiO_2 crystal lattice.[5] Fe doping can narrow the band gap of TiO_2, leading to a red-shift in the absorption spectrum.[6] Fe^{3+} can also act as a shallow trap for photogenerated electrons and holes, as its energy level is close to that of Ti^{3+}/Ti^{4+}, thus favoring the separation of photogenerated electron−hole pairs and improving quantum yield.[7] Furthermore, the introduction of Fe^{3+} ions into the crystal structure of TiO_2 has the potential to create and stabilize oxygen vacancies, leading to an effective photocatalytic capability.[8]

Various methods have been employed to introduce Fe^{3+} ions into TiO_2 lattices, including sol−gel,[9] hydrothermal,[10] and

Received: July 11, 2023
Revised: November 1, 2023
Accepted: November 9, 2023
Published: November 30, 2023

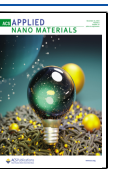

coprecipitation[11] techniques. While these methods demand prolonged reaction periods, often up to 24 h, flame spray pyrolysis (FSP) offers a faster alternative for producing metal oxide nanoparticles. In FSP, the metal-containing precursor is dissolved in a flammable solvent. This precursor solution is then atomized with oxygen and transformed into fine droplets. The heat and radicals from the flame lead to precursor decomposition and subsequently to the formation of typically oxidized particles of the element of interest.[12] FSP synthesis has advantages that include rapid synthesis (typically in the range of milliseconds), without the formation of liquid byproducts, easier collection of products, and fewer process steps.[12] However, FSP requires large amounts of atomizing gas and complex solvents that may limit the quality of the synthesized nanopowders.[13] The FSP process also depends on the atomization technique, which generates clouds of polydisperse droplets.[14]

To address these drawbacks, in this work, the precursor solutions were sprayed into the FSP by electrohydrodynamic atomization, which is termed electrospray-assisted flame spray pyrolysis (EAFSP). EAFSP enables the atomization of a liquid precursor without any shear flow and facilitates the adjustment of droplet size over a wide range.[15] Electrostatic forces propel the charged precursor droplets from the electrospray nozzle to the grounded flame, eliminating the need for a dispersion gas. Moreover, the electric charges on the droplets cause repulsive forces, which prevent droplet coalescence and coagulation.[14] It is worth noting that in most cases TiO_2 particles are synthesized using titanium alkoxide precursors, specifically titanium tetraisopropoxide (TTIP), as the Ti^{3+} precursor. However, the hydrolysis and condensation reactions of these precursors with water or even the atmospheric humidity can be violent without control,[16] leading to the formation of undesired products during the electrospraying of the precursor. To prevent such precipitation, in the presented work, titanium diisopropoxide bis(acetylacetonate) (TDIP) was used as a Ti^{3+} precursor. Indeed, the presence of two acetylacetone (AcAc) groups in TDIP can stabilize the solution formulation by inhibiting uncontrolled precipitation as the hydrolysis of the AcAc groups is suppressed.[17]

TiO_2 nanoparticles have been applied in the medical field due to their antibacterial activity. Antibiotic resistance is a growing issue that affects the entire world.[18] Indeed, in human medicine, resistance to pathogenic microbes and intracellular bacterial infections are challenging problems.[19] Antibiotics are then required for fighting these infections, but due to their poor solubility in aqueous media and/or stability in biological media, their vectorization is often needed[20−23] for (i) delivering the therapeutic agents at the required concentration specifically in the intracellular medium and (ii) avoiding antibiotic resistance.[24] Antibacterial carriers have then been proven to allow for avoiding/preventing antibiotic efflux and also increasing the intracellular retention of the antibiotic.[25]

Some particles can also be used as antibiotics because an entirely different antibacterial activity mechanism is implied compared to conventional antibiotics. It includes (i) disruption of the bacterial cell membrane integrity,[26] (ii) induction of oxidative stress due to free radical formation,[27] (iii) mutagenesis,[28] (iv) DNA and protein damage,[29] (v) inhibition of the replication of DNA by binding to DNA,[29] and (vi) respiratory chain disruption.[30]

One of the problems with the current antimicrobial material is related to its irritant action and high toxicity for humans. Developing a new strategy for the elaboration of cost-effective and safe biocide systems is therefore crucial. This is why we propose exploiting Fe-doped TiO_2 particles. Traditionally, TiO_2 particles are considered to be low-toxicity particles.[31] Due to this reason, they have often been employed as a "negative control" in a lot of *in vitro* and *in vivo* particle toxicological studies.[32] Fe has the ability to produce free radicals and enhance the oxidative stress of TiO_2 via Fenton reactions, which may result in an increased antibacterial activity. These findings highlight the potential of Fe-doped TiO_2 nanoparticles as effective antibacterial agents, particularly upon exposure to UV light.

Some Gram-negative and Gram-positive bacteria are highly resistant and then are difficult to treat pathogens.[33] The list of examples includes *Acinetobacter*, *Pseudomonas aeruginosa*, *Klebsiella*, and even *Escherichia* species as Gram-negative bacteria[34] and methicillin-resistant *Staphylococcus aureus* as Gram-positive bacteria.[35] Consequently, there is an increasing effort to implement new antibiotic analogues and identify new antibacterial therapeutics.[36] Spectinomycin is a broad-spectrum antibiotic with moderate activity against both Gram-negative and Gram-positive bacteria (e.g., useful for the treatment of gonorrhea infections). Spectinomycin contains the 1,3-dibasic sugar actinamine and therefore is classified structurally with the aminoglycoside antibiotics (i.e., neomycins, kanamycin, etc.). Spectinomycin, like the other aminoglycosides, inhibits protein synthesis in *Escherichia coli* by interfering with the function of the 30S subunit of the ribosome.[37] However, unlike other aminoglycosides, it does not induce detectable misreading (amino acid substitution) during polypeptide synthesis *in vitro*. Spectinomycin-resistant bacteria have recently merged. Resistance to spectinomycin is often caused by enzymes that inactivate the drug by adenylylation.[38]

In this article, pure and Fe-doped TiO_2 nanoparticles were initially synthesized by the EAFSP method. In this regard, various *in situ* and *ex situ* diagnostics such as phase-Doppler anemometry (PDA), high-speed shadowgraphy, spICP-MS, SMPS, SAXS, Raman, TEM, etc., were applied for analyzing the in-flight droplet characteristics in the spray as well as primary and agglomerate nanoparticle evolution within the process. The results lead to optimized production parameters for a particle structure suited as antibiotic analogues. Then, we investigated the impact of these particles on the growth of bacteria resistant to antibiotics, namely, spectinomycin-resistant *Escherichia coli*.

2. EXPERIMENTAL SECTION

2.1. Materials. All chemicals and solvents were reagent grade and used without further purification. Titanium diisopropoxide acetylacetonate (TDIP, 75 wt % in isopropanol), titanium(IV) bis(ammonium lactato)dihydroxide (TALH) (50 wt % in H_2O), iron(III) acetylacetonate ($Fe(acac)_3$), and ethanol (EtOH) were purchased from Sigma-Aldrich.

2.2. Synthesis of Pure and Fe-Doped TiO_2 Nanoparticles. In this work, pure and Fe-doped TiO_2 nanoparticles were synthesized by the electrospray-assisted flame spray pyrolysis (EAFSP) method. Titanium diisopropoxide bis(acetylacetonate) (TDIP) and iron acetylacetonate ($Fe(acac)_3$) were used as Ti^{4+} and Fe^{3+} precursors, respectively, and EtOH was used as a solvent. To produce pure TiO_2 nanoparticles, various amounts of TDIP were mixed with EtOH to obtain the precursor solutions with Ti^{4+} concentrations of 0.5, 1, and 1.5 M. The synthesized nanoparticles will be denoted as TiO_2-*x*, where *x* represents the initial Ti^{3+} concentration of the precursor. To produce Fe-doped TiO_2, $Fe(acac)_3$ was added to the TDIP solution to give the desired Fe^{3+} to Ti^{4+} ratio. Three different molar ratios of Fe^{3+} to Ti^{4+} were used: 1, 5, and 10% Fe/Ti molar ratio of Fe/Ti. In these experiments, the Ti^{4+} concentration was kept constant at 1.5 M. For

https://doi.org/10.1021/acsanm.3c03107
ACS Appl. Nano Mater. 2023, 6, 22660−22672

simplicity, the resulting particles will be denoted as *y*% Fe-doped TiO_2, where *y* represents the molar ratio of Fe^{3+} to Ti^{4+}.

The experimental setup was conceptually similar to that recently reported.[13,39] In short, the SPP1980 SpraySyn burner was used as a lab-scale standard burner.[40] Figure 1 displays the schematic diagram of the

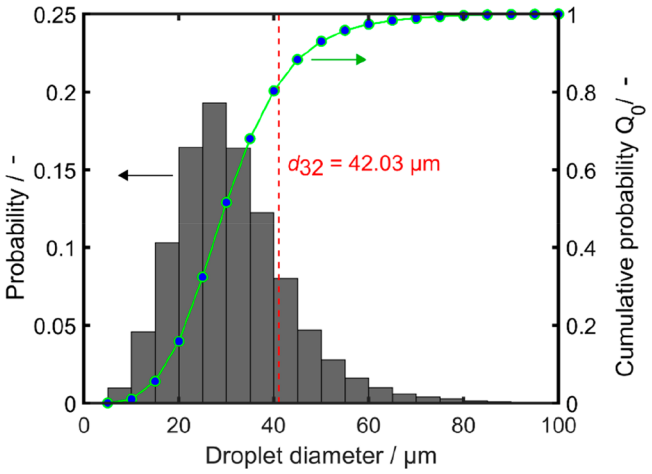

Figure 1. Initial droplet size distribution and cumulative probability density distribution Q_0 of the TDIP solution.

EAFSP setup. The burner was operated with 0.8 L min^{-1} methane (purity of 2.5, Linde AG, Germany) and 2.0 L min^{-1} oxygen (purity of 2.5, Linde AG, Germany) to generate the pilot flame. A pressured sheath air coflow (approximately 11 L min^{-1}) was used for flame shaping, especially for stabilizing the flame due to the low fuel gas velocities. As detailed in our previous work,[13] temperature profiles of the flame were recorded from 40 to 290 mm heights above the burner (HAB) using a Type-K thermocouple. Because of the relatively low flow rates of the gaseous fuels, the temperatures recorded were moderate. Specifically, at an HAB of 40 mm, the temperature reached 1400 °C, while at an HAB of 290 mm, it was approximately 300 °C. Here, the electrospray unit was fixed near the flame setup with a fixed horizontal distance of 40 mm. Then, using a syringe pump (KD Scientific Gemini 88), the resulting precursor solutions were transferred to a metallic nozzle (0.41 mm ID, 0.72 mm OD, Nordson 7018263) under a constant feed rate of 50 µL/min. Simultaneously, a high-voltage power supply (Fug HCN350-12500) was operated at 2.7 kV for the atomization of the precursor solution. The torch itself was grounded. Consequently, the positively charged droplets were accelerated toward the grounded flame environment. Then, the nanoparticles were produced by the reaction in the flame region. The resulting nanoparticles were collected on the 155 mm glass fiber filter located at 450 mm HAB with the aid of a vacuum pump. For the direct comparison between *ex situ* measurements (such as TEM, BET, and SAXS) and *in situ* measurements (like SMPS and spICP-MS), the as-synthesized samples were not subjected to any postheat treatments. On the other hand, for the investigation of the impact of Fe doping, evidenced by XRD, Raman, and UV−vis spectroscopy measurements, as well as for antimicrobial applications assessments, the samples were subjected to a postheat treatment at 500 °C for 2 h in the air to enhance crystallinity.

2.3. Assay for Antibacterial Activity. *Microbial cultures.* Spectinomycin-resistant *Escherichia coli* was grown aerobically at 37 °C for 24 h in a liquid medium. For the assay, 500 µL of bacterial suspension was added to 5 mL of the culture medium, and then 5.5 mL of the suspension of the particle (final particle concentration 0.4 mg/mL) was added (incubated under agitation at 37 °C). As a reference, a suspension of bacteria without particles was used (only water was added in the same amount of the added suspension of the particle). Bacterial growth was monitored in dark or under UV light (365 nm) every hour by reading the optical density of bacterial suspensions at 630 nm using a UV−vis spectrophotometer. To be more precise, the UV treatment was performed using the Fusion SL 3500WL/LC XPress device, which involves the use of tubes with the following characteristics: 2 × 8 W 365 nm tubes.

The percentage of inhibition (I (%)) was estimated using eq 1:

$$I\ (\%) = 100 - \left(\frac{OD_{sample}}{OD_{reference}} \times 100\right) \quad (1)$$

where OD_{ref} and OD_{sample} correspond to the optical density (OD) of the reference (suspension of bacteria) and sample (suspension of bacteria containing a suspension of the sample), respectively. It should be noted that the antibacterial test has been done 2 times.

2.4. Samples Characterization. The droplet size of the electrospray at the capillary outlet was measured via the nonintrusive 1D phase-Doppler anemometry (PDA) method. The combustion processes of precursor droplets were recorded *in situ* with a high-speed camera. The growth of primary and agglomerate nanoparticles along the flame was evaluated *in situ* by a scanning mobility particle sizer (SMPS, Model 3938, TSI) equipped with a soft X-ray aerosol neutralizer (Model 3088, TSI), a 1 nm DMA (differential mobility analyzer, Model 3082, TSI), a nanoenhancer (Model 3757, TSI), and a condensation particle counter (Model 3750, TSI). In this regard, particle sampling was conducted by the hole-in-a-tube method, which is described in detail in the Supporting Information. A commercial inductively coupled plasma mass spectrometer (ICP-MS/MS 8900 triple quadrupole by Agilent) was used as an analytical tool for particle mass determination. To examine the structure and morphology of the particles obtained, both transmission electron microscopy (TEM, JEOL JEM2100, 160 kV) and scanning electron microscopy (SEM, Zeiss DSM Gemini 982, 5 kV) were utilized. The X-ray diffraction (XRD) pattern was measured with an X-ray diffractometer (Empyrean, Malvern Panalytical) with a germanium monochromated Cu Kα radiation (λ = 1.54056 Å) in the Bragg−Brentano configuration. Small-angle X-ray scattering (SAXS) measurements were performed with the laboratory camera Xeuss 2.0 Q-Xoom (Xenocs SA, Grenoble, France) with a Bonse−Hart module for USAXS (Ultra SAXS). Nitrogen adsorption−desorption isotherms were recorded with an ASAP 2020 from Micromeritics GmbH. The Brunauer−Emmett−Teller (BET) method was utilized to calculate the specific surface area. The Raman spectrum was obtained using a WITec alpha300R confocal Raman instrument at room temperature. UV−vis absorption spectroscopy (SPECORD 200, Analytik Jena) was used to analyze the absorbance spectra of the nanomaterials over the wavelength range from 200 to 700 nm at room temperature. The optical gap was calculated by the Tauc plot.[41]

Detailed information regarding the experimental setup for the high-speed camera, PDA, SMPS, XRD, and SAXS measurements is described in the Supporting Information.

3. RESULTS AND DISCUSSION

3.1. Synthesis of Pure TiO_2 Nanoparticles. In the first experiment, pure TiO_2 nanoparticles were produced by using the EAFSP method. The precursor solutions containing different Ti^{4+} concentrations were electrosprayed using the power supply to the grounded flame. In the flame region, nucleation and growth processes of TiO_2 nanoparticles may occur following precursor evaporation (gas-to-particle transition) or inside the liquid droplet (droplet-to-particle transition).[42,43] To investigate the formation process of TiO_2 nanoparticles, various *in situ* and *ex situ* diagnostics were applied for analyzing droplet characteristics as well as primary and agglomerate nanoparticles evolution within the process (Scheme 1).

3.1.1. In Situ Droplet Characterization. The examination starts with *in situ* measuring of the initial droplet size distribution of the electrospray at the capillary outlet by PDA measurement (Figure 1). As shown in Figure 1, a unimodal droplet size distribution is formed, resulting in droplets with a Sauter mean

https://doi.org/10.1021/acsanm.3c03107
ACS Appl. Nano Mater. 2023, 6, 22660−22672

Scheme 1. Schematic of the Experimental EAFSP Setup and Process Diagnostics for Analyzing the Consecutive Stages of TiO_2 Nanoparticles Evolution

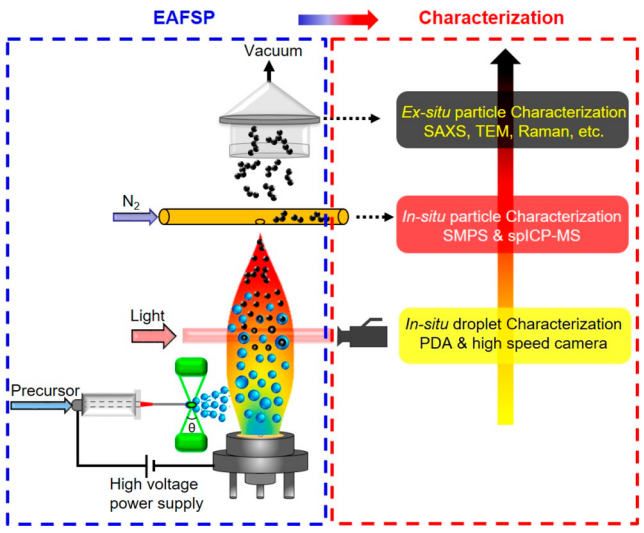

diameter d_{32} of 42.03 μm. The droplet size distribution follows a log-normal distribution with the respective parameters (σ-logarithmic standard deviation and μ-location parameter) printed in Figure 1. The fine electrospray is injected horizontally into the flame, and the droplets enter the flame by their initial momentum as well as by the entrainment of air from the surroundings.

Furthermore, the combustion of precursor droplets within the flame reactor was visualized by high-speed shadowgraphy. As already proven by single droplet experiments and conventional FSP experiments, μ-explosions effectively enhance droplet evaporation and precursor release.[44−47] It is supposed that there is a link between the homogeneity of the produced powder and the existence of μ-explosions as droplets disintegrate cascade-wise until complete evaporation. High-speed shadow spectral images of the electrospray flame with a feed rate of 50 μL min^{-1} were recorded to investigate the dynamics of charged precursor droplets in flames, revealing highly frequent μ-explosions. Two exemplary samples are displayed in Figure 2 with a temporal resolution of 10 μs. The onset of μ-explosions is

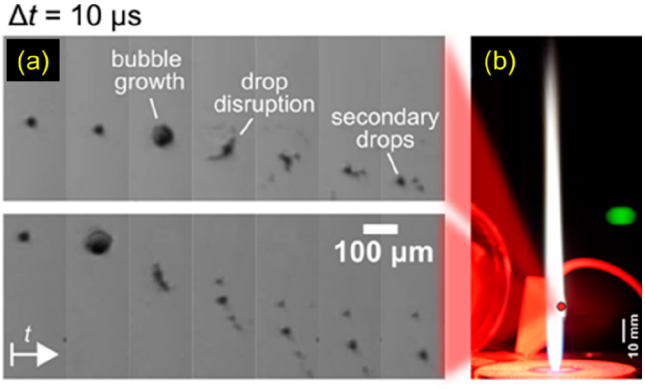

Figure 2. (a) Sequences of TDIP based precursor droplet μ-explosions inside the electrospray flame at HAB = 30 mm at a radial position of r = 2 mm. (b) Photography of the electrospray flame. Note the red dot indicating the measurement location and electrospray needle is not shown here.

initiated with the formation of vapor bubbles inside the droplet. The ongoing evaporation inside the droplet results in droplet surface instabilities until the pressure forces overcome the forces of surface tension. The droplets disrupt clouds of numerous secondary droplets with intense precursor release. The corresponding high-speed camera recorded videos are shown in the Supporting Information Video S1.

3.1.2. In Situ Particle Characterization. After the precursor droplets are electrosprayed in the flame, the process of particle formation starts with nucleation and continues to grow through a collision-coalescence mechanism. As the flame temperature drops, aggregates or agglomerates are formed as a result of the characteristic coalescence time increasing substantially. In this regard, an SMPS was coupled with the experimental EAFSP setup to *in situ* evaluate the growth of primary and agglomerate nanoparticles along the flame. The particle sampling was conducted by the hole-in-a-tube method, which is described in detail in the Supporting Information. Figure 3a−c represents the particle size distribution measurements as a function of HAB for as-synthesized TiO_2-0.5, TiO_2-1.0, and TiO_2-1.5 nanoparticles, respectively. It should be noted that the HAB does not take into the position of the electrospray account; i.e., the distance between the electrospray unit and the flame was fixed at 20 mm HAB. As shown in Figure 3a−c, all three TiO_2 nanoparticles have narrow size distributions at their lowest HABs, where the sampling was done within or close to the flame. However, when measurements were performed at higher HAB, the size distribution became wider and was shifted significantly toward larger values. This indicates that the particle growth process occurs outside the flame region. We attribute this to the extended sintering times experienced by particles that remain longer in the high-temperature zones of flame. Conversely, when the HAB is lower, the resulting particles are generally smaller and display a narrower size distribution. Indeed, the HAB can significantly influence the particle size distribution. This is predominantly due to the variation in the high-temperature residence time (HTRT) within the aerosol. Differences in HAB lead to changes in the characteristics of flame, such as its temperature, which in turn impacts factors like particle sintering time and coagulation rate.[48,49] The arithmetic mean diameter (AMD) along the axis of the nozzle centerline is illustrated in Figure 3d. The diameters of the arithmetic mean were increased linearly throughout the entire HAB range, resulting in an AMD of approximately 7−10 nm at 260 mm HAB. In addition, higher Ti^{4+} precursor concentrations lead to higher AMDs. One possible explanation for this behavior is that the increased concentration of precursor in the solution results in a greater number of nucleation seeds in the spray flame, which can lead to higher coagulation rates and the formation of larger, denser agglomerates of primary particles.[44]

Moreover, single-particle ICP-MS (spICP-MS) measurements were conducted to obtain insights into the EAFSP process that causes various particle morphologies. Because spICP-MS nanoparticle analysis reveals the mass of an aerosol particle, a preclassification by DMA opens up the chance of determination of different particle morphologies, judged by its mass signal in spICP-MS analysis. Further information regarding the coupling of an aerosol process to an spICP-MS system and the data evaluation regarding the differentiation between fractal-like particles and solid spheres have been recently reported by Bierwirth et al.[50] As described for the SMPS measurements of nanoparticles, the hole-in-a-tube sampling was applied for spICP-MS analyses as well to transfer particles from the flame

https://doi.org/10.1021/acsanm.3c03107
ACS Appl. Nano Mater. 2023, 6, 22660−22672

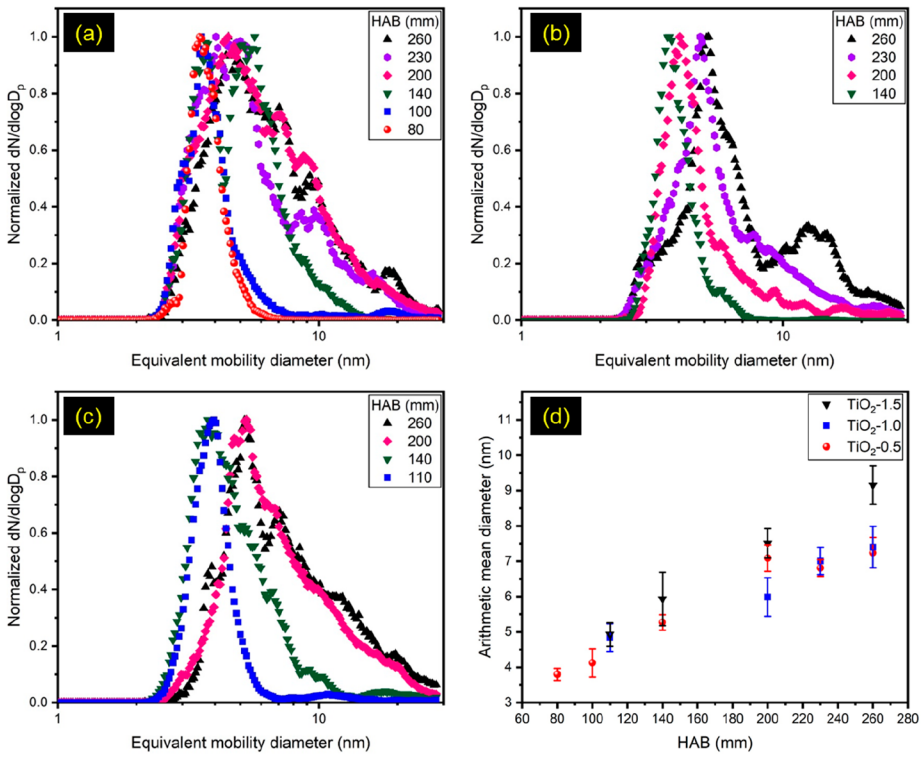

Figure 3. Normalized particle number size distribution along the flame for different HABs on the central axis obtained by SMPS for as-synthesized (a) TiO_2-0.5, (b) TiO_2-1.0, and (c) TiO_2-1.5 nanoparticles and (d) the corresponding arithmetic mean diameters.

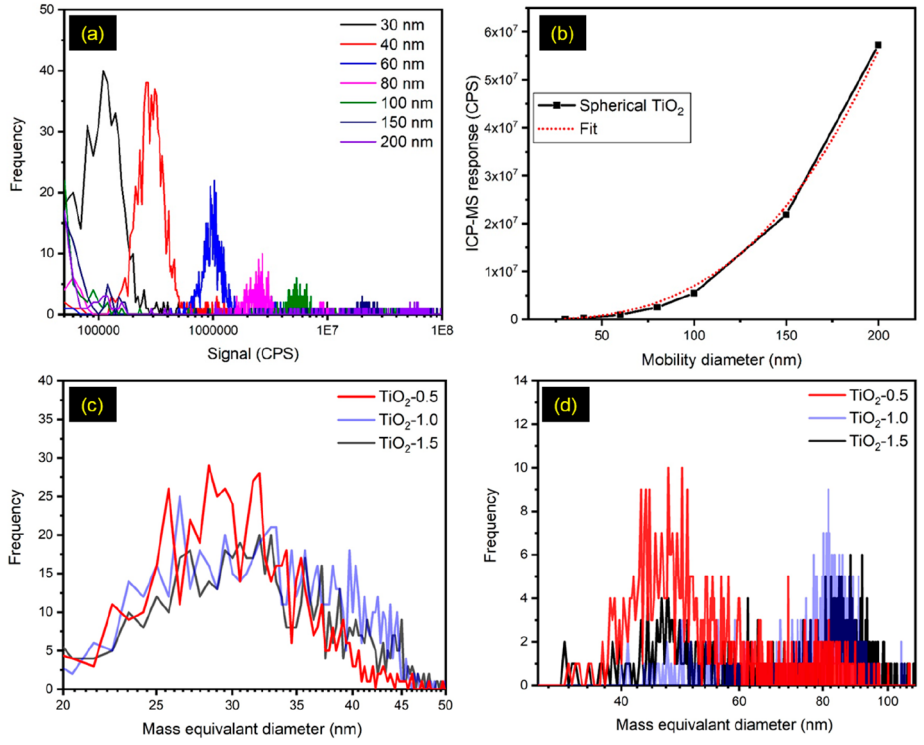

Figure 4. (a) Signal distribution for solid TiO_2 nanoparticles classified at distinct mobility equivalent particles sizes (d_{Mob} = 30−200 nm, CPS: counts per second; the graph represents data for the mass 48 u, corresponding to Ti). (b) Center-of-mass signal distribution over mobility equivalent particle size indicating the cubic dependency of mass and size as the calibration for TiO_2 nanoparticles. (c) Signal distribution of as-synthesized 50 nm TiO_2 sampled from the EAFSP. The *x*-axis has been transformed to an equivalent mass diameter by the preliminary found calibration factor. The legend refers to the chosen molar Ti^{4+} precursor concentration. (d) Signal distribution for the as-synthesized 90 nm TiO_2 nanoparticles.

into the spICP-MS. It should be noted that for an *in situ* particle analysis by spICP-MS, a gas phase calibration with aerosol particles of known shape and mass is necessary. Hence, a spray-drying setup was initially deployed to produce solid, spherically

https://doi.org/10.1021/acsanm.3c03107
ACS Appl. Nano Mater. 2023, 6, 22660−22672

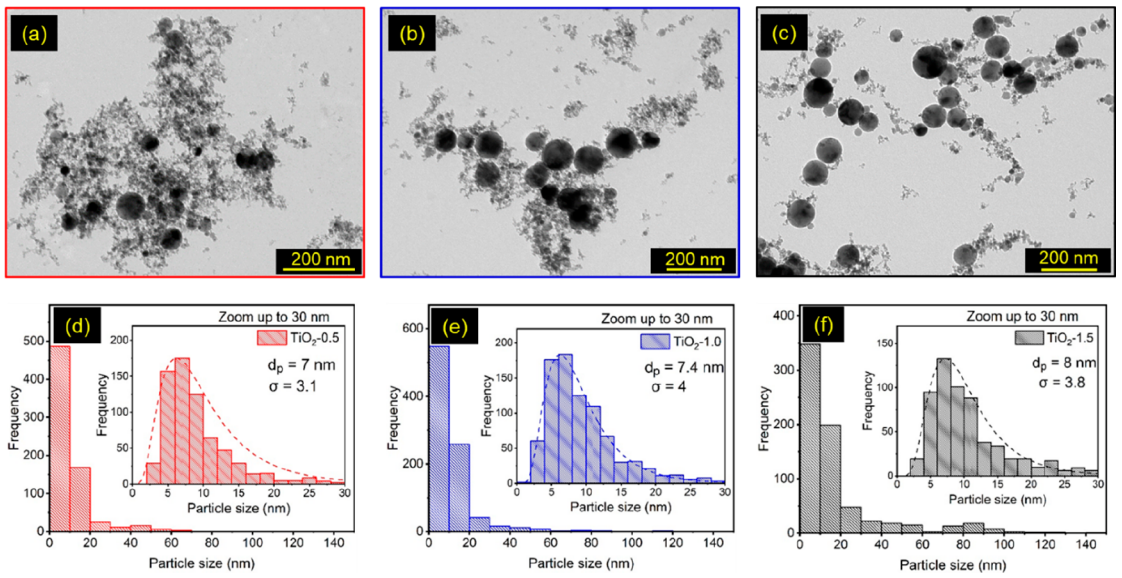

Figure 5. TEM micrographs and corresponding particle size distribution histograms of (a, d) as-synthesized TiO_2-0.5, (b, e) TiO_2-1.0, and (c, f) TiO_2-1.5 nanoparticles.

shaped TiO_2 nanoparticles that can be size-classified by a DMA for further mass analysis by spICP-MS. To this end, a water-soluble Ti^{4+} precursor (TALH) was used to produce TiO_2 nanoparticles by spraying and subsequent calcination in a tube furnace, as the experimental procedure was discussed in the Supporting Information. The TEM and SEM images (Figure S1) show that the synthesized particles are solid and spherical in shape. The mass response, at mass 48 u, caused by different classified particle sizes ($d_{DMA} \triangleq d_{Mob}$) introduced into the spICP-MS is shown in Figure 4a. An increased particle size comes along with a higher particle mass, determined by $m_P = \frac{\pi}{6} d_{Mob}^3 \rho_P$. Thus, the center of each mass distribution shown in Figure 4a was plotted against the chosen mobility diameter, d_{Mob} (Figure 4b). The dependency of $m_P \propto d_{Mob}^3$ becomes clearly visible. At this point, a certain mass response by unknown aerosol particles can be related to a mass-equivalent particle size by using the calibration curve from Figure 4b. Hence, spICP-MS is calibrated for TiO_2 aerosol particles. In this work, the hole-in-a-tube particle sampling from the EAFSP guarantees the desired low particle concentration (ideally less than 1 particle/ccm) that is required for spICP-MS measurements. The mass signal distributions of as-synthesized TiO_2 nanoparticles produced using various Ti^{4+} precursor concentrations for two different classified particle sizes of d_{Mob} = 50 and 90 nm are shown in Figures 4c and 4d, respectively. It becomes evident that fractal-like particles in the size class of 50 nm always exhibit the same mass response, hence a comparable particle structure as will be discussed by TEM analysis. From Figure 4c it can be concluded that nonspherical particles have formed because preclassified particles with d_{Mob} = 50 nm exhibit a peak response at around 30 nm. Spherical particles would, in contrast, exhibit a signal response close to 50 nm, as shown in Figure 4c. The spICP-MS reflects this observation by a monomodal signal distribution, as shown in Figure 4c. An increased TDIP concentration does not change the particle morphology in the aforementioned size class. An altered behavior becomes visible by adjusting the classified size from d_{Mob} = 50 to 90 nm at the DMA. While a low TDIP concentration causes a high number of fractal-like particles (see red profile in Figure 4d), an increased concentration enables the formation of solid TiO_2 spheres (blue and black profiles in Figure 4d). In Figure 4d, the morphology of an analyzed particle can be derived based on the initial size classification (here 90 nm) and the response by spICP-MS based on the fact that the second peak in the signal distribution (blue and black profiles) shows up at a size close to 90 nm. As derived from the spICP-MS calibration, a 90 nm signal in the mass signal distribution can be solely caused by spherical, solid particles. Hence, it can be concluded that two different particle morphologies coexist in the size class of d_{Mob} = 90 nm, fractal-like particles and spherical particles, at the same time. Moreover, these findings will be supported by offline TEM imaging in the following. Consequently, spICP-MS measurements may open up the option of an *in situ* determination of the particle formation route (droplet-to-particle for spherical particles and gas-to-particle for fractal-like particles) in dependence on chosen synthesis conditions such as precursor concentration.

3.1.3. Ex Situ Particle Characterization. The effect of the Ti^{4+} concentration in the precursor on the formation of TiO_2 nanoparticles is revealed by TEM micrographs. Figure 5a–c shows the TEM images of as-synthesized TiO_2-0.5, TiO_2-1.0, and TiO_2-1.5 nanoparticles, respectively. Furthermore, their corresponding particle size distributions were derived from TEM data by using ImageJ, and the histograms are provided in Figure 5d–f. The TEM micrographs indicate that all three TiO_2 nanoparticles consist of mostly fractal-like agglomerates and fine particles (sizes up to 30 nm), with the mean primary particle sizes (d_p) around 8 nm. However, a few large spherical particles of up to 150 nm were observed for all materials. Furthermore, the amount of these large spherical particles increases by increasing the concentration of Ti^{4+} precursor, which is in close agreement with the spICP-MS results. Generally, spray-flame synthesis produces particles via two mechanisms: the formation of fine nanoparticles is originated from the gas-to-particle conversion, whereas the formation of large spherical nanoparticles is assumed to result from the droplet-to-particle conversion.[42,43] It has already been proposed that when the solvent is more volatile than the precursor, solvent evaporation from the droplet surface will cause a reduction in the solvent concentration, leading to the precipitation of the precursor and

https://doi.org/10.1021/acsanm.3c03107
ACS Appl. Nano Mater. 2023, 6, 22660–22672

the formation of a viscous shell. The heating of the droplet and the subsequent solvent evaporation inside the shell can cause a pressure buildup, which may result in μ-explosions, as observed in Video S1.[51,52] In this study, while the finer particles are derived from the gas-to-particle conversion, the larger nanoparticles are believed to form via the droplet-to-particle mechanism, stemming from small secondary droplets produced by μ-explosions. Higher precursor concentrations tend to promote viscous shell formation and surface decomposition of droplets, leading to a greater number of large particles. It is worth noting that in precursor systems without μ-explosions, average nanoparticle sizes can sometimes reach the micrometer scale. Furthermore, as previously mentioned, the presence of charge on the droplets has the potential to enhance the evaporation process by reducing the surface tension and even inducing droplet μ-explosions.[39] Therefore, the disintegration of large precursor droplets into small particles would occur because of the μ-explosions.

The textural properties of as-synthesized TiO_2-0.5, TiO_2-1.0, and TiO_2-1.5 nanoparticles were characterized by N_2 adsorption−desorption measurements (Figure S2). All particles show classical type IV isotherms with H3-type hysteresis loops, indicating that the pore originates from random aggregation of nanoparticles. The calculated BET specific surface area (SSA) of resulting samples is summarized in Table 1. It was observed that for the TiO_2-0.5 sample, the SSA was the highest with a value of 70 m^2/g while it dropped to 48 and 38 m^2/g for TiO_2-1.0 and TiO_2-1.5 nanoparticles, respectively, as a result of a higher amount of large spherical particles.

Table 1. Characteristics of the Primary Particles and Aggregates Derived from SAXS Data and SSA by BET

sample	SAXS d_{Rg1} [nm]	SAXS d_{g2} [nm]	SAXS p_3 [−]	SAXS SSA [$m^2\ g^{-1}$]	BET SSA [$m^2\ g^{-1}$]
TiO_2-0.5	8.2	76.9	1.7	94.5	70
TiO_2-1.0	10.9	120.5	2.0	51.9	48
TiO_2-1.5	13.9	145.8	1.6	42.4	38

As an integral measurement technique, SAXS can provide information about the particle structure, such as the primary particles and the shape of the aggregates. Figure 6a shows the merged scattering data of 2 different sample−detector distances (2500 and 80 mm) and USAXS data for the as-synthesized TiO_2-0.5, TiO_2-1.0, and TiO_2-1.5 samples. The scattering data are divided into 3 structural levels starting with the smallest scattering objects at the largest scattering vector q: the first level for the small primary particles, the second for the larger primary particles, and the third for the aggregates. For better legibility, the scattering data are displayed in arbitrary units with the lowest concentration as the lowest curve. Additionally, the local Guinier and power law fit of the unified fit are indicated underneath or above the corresponding data.

As evident in the TEM and spICP-MS analyses, this particle system shows a bimodal distribution in the primary particles, with both peaks shifting to larger particle sizes with higher precursor concentrations. The same behavior is found in the SAXS data in Figure 6a: Each curve shows two significant changes in the slope, which marks the region for a Guinier fit. With increasing precursor concentration, both Guinier fits shift to a smaller scattering vector q, indicating an increase in the particle size. The calculated diameters d_{Rg1} for the smaller primary particles using eq S6 and d_{g2} for the larger primary particles using eq S5 are listed in Table 1. Despite the USAXS measurement, the resolution of the scattering vector q is not sufficient to show a Guinier region for the aggregate size. In regards to the fractal properties, level 3 displays the fractal structure of the aggregates in the slope p_3 with values between 1.6 and 2.0 (see Table 1). This indicates a flaky shape, which is very typical for flame-made products.[53,54]

To gain detailed information about the bimodal behavior of the primary particles, size distributions were calculated from the SAXS data of the first and second structural levels using the model size distribution of the program IgorPro. Figure 6b shows the resulting volume size distributions for primary particles of the three precursor concentrations. In agreement with the results of TEM, spICP-MS, and SAXS, all three distributions exhibit bimodal behavior with a shift to larger particles with increasing precursor concentration. The first peak is always significantly higher than the second one. The amplitude ratio between the two peaks decreases with increasing precursor concentration, indicating a decrease in the concentration of smaller primary particles (level 1) with higher precursor concentrations. Overall, the peak diameters are in good agreement with the diameters d_{Rg1} and d_{g2} calculated from the unified fit parameters. Additionally, the volume-based results from SAXS were converted into number-based data, allowing for a direct comparison with the results from TEM, spICP-MS, and SMPS, as shown in Figure S3. The converted results further confirm that as the precursor concentration increases, the

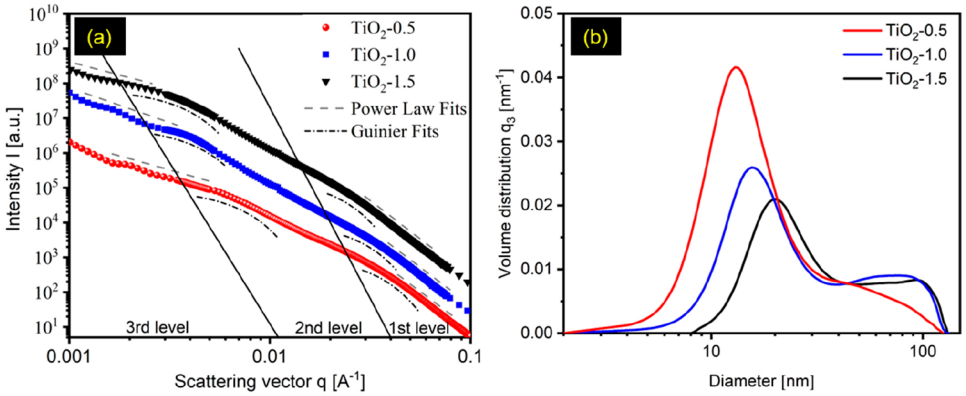

Figure 6. (a) SAXS scattering data and local fits and (b) volume size distribution calculated from the SAXS data of as-synthesized TiO_2-0.5, TiO_2-1.0, and TiO_2-1.5 nanoparticles.

https://doi.org/10.1021/acsanm.3c03107
ACS Appl. Nano Mater. 2023, 6, 22660−22672

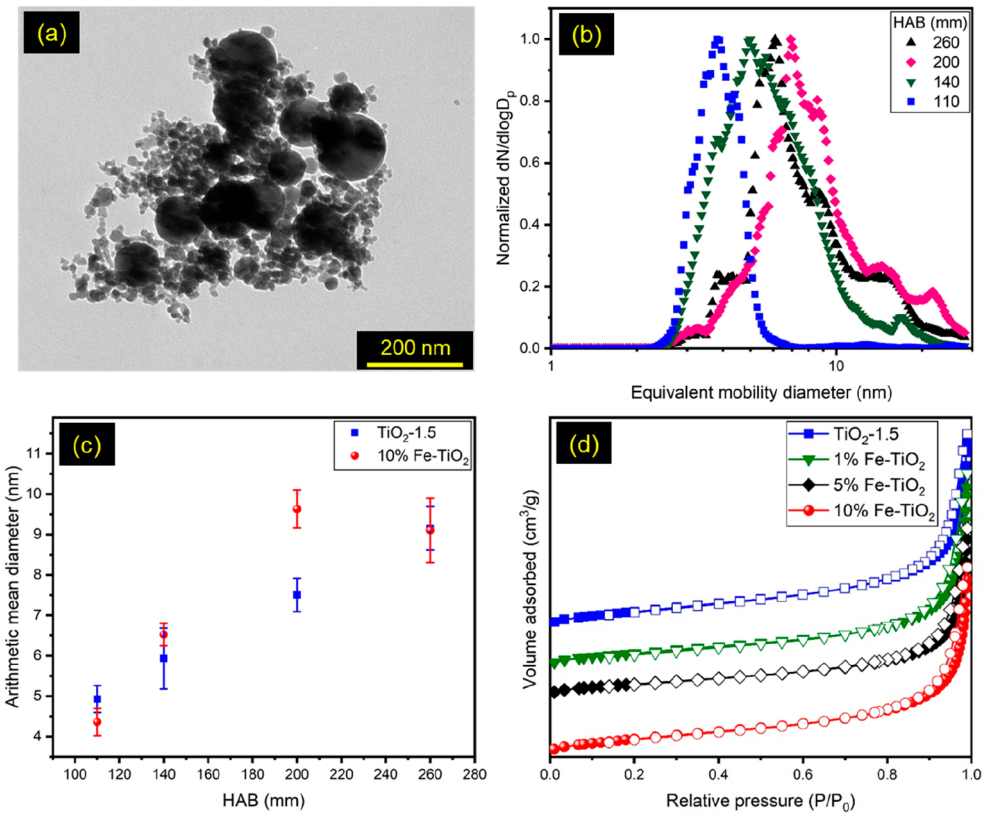

Figure 7. (a) TEM images of as-synthesized 10% Fe−TiO_2, (b) normalized particle number size distribution along the flame for different HABs on the central axis obtained by SMPS for as-synthesized 10% Fe−TiO_2 nanoparticles, (c) arithmetic mean diameter of as-synthesized TiO_2-1.5 and 10% Fe−TiO_2 nanoparticles, and (d) nitrogen adsorption−desorption isotherms of as-synthesized TiO_2-1.5 and Fe-doped TiO_2 samples.

number size distributions tend to shift toward larger particles. However, it is noteworthy to mention that the pronounced peaks corresponding to the larger particles become less evident in this representation due to their relatively low number concentration.

Using eq S7 for the displayed range of the scattering vector q = 0.001−0.1 A^{-1} in Figure 6a, the specific surface area (SSA) is determined and can be compared to BET results because both fractions of the primary particles are included (see Table 1).

The characterization results presented above provided valuable insights into the droplet characteristics, primary and agglomerate nanoparticle evolution, and the particle formation route under varying synthesis conditions. These results provide a fundamental understanding of the pure TiO_2 nanoparticles and serve as a critical foundation for our investigation of Fe-doped TiO_2 nanoparticles. By establishing a baseline for the properties and behavior of pure TiO_2 nanoparticles, we can now analyze and compare the effects of Fe doping on crucial parameters such as the crystallite size, phase formation, oxygen vacancies, and optical gap energy. Such a comparative analysis will enable us to assess the potential enhancements and changes introduced by Fe doping and better understand the mechanisms underlying the antibacterial activity of the Fe-doped TiO_2 nanoparticles.

3.2. Synthesis of Fe-Doped TiO_2 Nanoparticles. To form an antibacterial agent, Fe was found to be a promising material. A TiO_2 matrix is desired to introduce it into the human body. Therefore, we produced Fe-doped TiO_2 nanoparticles using the EAFSP method. In this regard, the precursor solutions containing Fe^{3+}/Ti^{4+} molar ratios corresponding to 1, 5, and 10% were electrosprayed onto the flame. The Ti^{4+} concentration was kept constant at 1.5 M for all experiments. The morphology of the Fe-doped TiO_2 nanoparticles synthesized in this study was characterized by using TEM. Figure 7a displays the TEM image of as-synthesized 10% Fe−TiO_2 nanoparticles, while Figure S4 shows the TEM images of as-synthesized 1% Fe−TiO_2 and 5% Fe−TiO_2 nanoparticles. The results suggest that the particle morphology of Fe-doped TiO_2 samples is comparable to that of the TiO_2-1.5 case.

Furthermore, the primary particle size distribution of the as-synthesized 10% Fe−TiO_2 nanoparticles was examined by SMPS to determine its evolution as a function of HAB, as depicted in Figure 7b. The HAB was varied between 110 and 260 mm, and it was observed that small particles with narrow size distributions were formed at 110 mm HAB. With increasing HAB, the size distribution of particles became wider and shifted toward larger values. Figure 7c illustrates the corresponding AMD along the nozzle centerline axis, which increased with increasing HAB. Interestingly, it was found that the particle size did not vary much with the addition of Fe in the TiO_2 sample. The N_2 adsorption−desorption isotherms of all as-synthesized Fe-doped particles reveal a typical type IV isotherm with H3-type hysteresis loops, which is similar to that of a pure TiO_2 sample (Figure 7d). The calculated BET specific surface areas of as-synthesized 1% Fe−TiO_2, 5% Fe−TiO_2, and 10% Fe−TiO_2 are 34, 28, and 35 m^2/g, respectively. The obtained results suggest that the addition of Fe dopants did not significantly affect the primary particle size and surface area of the TiO_2 nanoparticles. This observation could be attributed to the relatively smaller ionic radius of Fe dopants compared with Ti^{4+} ions. However, it should be noted that the presence of Fe dopants can have a significant impact on other physicochemical

https://doi.org/10.1021/acsanm.3c03107
ACS Appl. Nano Mater. 2023, 6, 22660−22672

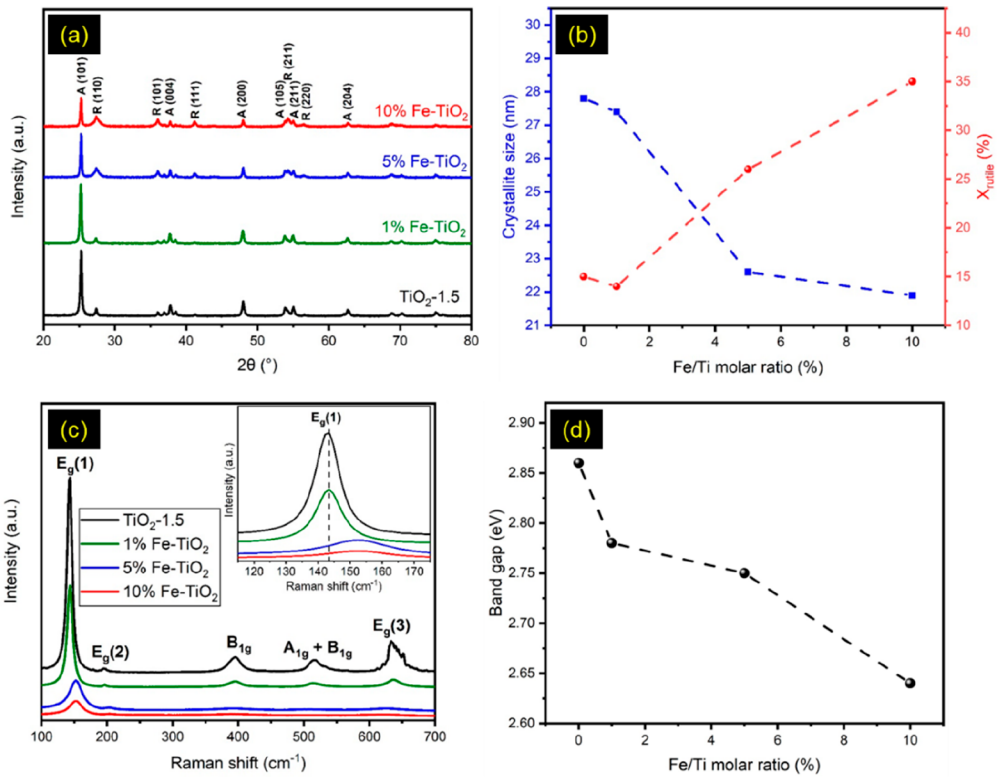

Figure 8. (a) XRD patterns of calcined TiO_2-1.5 and Fe-doped TiO_2 samples. (b) Crystallite size and the corresponding rutile weight fraction as a function of the concentration of Fe doping. (c) Raman spectra of calcined TiO_2-1.5 and Fe-doped TiO_2 samples. (d) Optical optical gap energy as a function of the concentration of Fe^{3+} doping.

properties of TiO_2 nanoparticles, which will be elaborated on in the subsequent discussion.

The crystal structures of the samples were investigated by an X-ray diffractometer. Figure S5 reveals an increase and sharpening in the intensity of the XRD peaks for the as-synthesized TiO_2-1.5 sample following heat treatment, suggesting improved crystallinity. Furthermore, the average size of the as-synthesized TiO_2-1.5 crystals increased slightly from 26 nm to around 28 nm after postheat treatment. Figure 8a shows the XRD pattern for calcined Fe-doped samples compared to that of calcined pure TiO_2-1.5 nanoparticles. All the samples exhibited mixed crystalline phases of anatase (JPCDS No. 21-1272) and rutile (JPCDS No. 21-1276) TiO_2.[55] Notably, no Fe segregation or formation of a new crystallite phase is observed, indicating that the Fe ions are effectively incorporated into the TiO_2 lattice framework. Because Ti^{4+} (0.68 Å, hexacoordination) and Fe^{3+} (0.64 Å, hexacoordination) have nearly similar ionic radii with the same coordination number, the substitution of Ti^{4+} by Fe^{3+} ions is highly feasible during the bottom-up flame synthesis.[56]

The average crystallite sizes (eq S1) and the rutile fraction present (X_{rutile}%) (eq S2) in the structures of the calcined pure TiO_2-1.5 and Fe-doped TiO_2 samples are shown in Figure 8b. It was observed that the average crystallite size decreased with an increase in the Fe^{3+} content in the samples. As Fe $^{3+}$ ions are substitutionally doped in TiO_2, to some extent, structural defects will be introduced into the crystal lattice of TiO_2 due to the slight difference in ionic radii of Ti^{4+} and Fe^{3+}. This lattice deformation consequently leads to restraint of the crystallite growth of Fe–TiO_2 grains and a decrease in the average crystallite size.[57]

Moreover, it was found that increasing the Fe^{3+} dopant concentration promotes the formation of the rutile phase percentage (Figure 8b). There are two suggested reasons responsible for this result.[58−61] One possible reason is that when tetravalent Ti^{4+} ions are substituted with trivalent Fe^{3+} ions, oxygen vacancies would arise spontaneously to retain charge neutrality. Because oxygen vacancies carry a positive charge, Fe^{3+} ions tend to be incorporated in the rutile phase, which has greater tolerance than anatase toward oxygen vacancies. The other suggested reason is that the smaller ionic radius of Fe^{3+} caused the compaction of the TiO_2 lattice and the creation of a denser rutile phase (ρ_{rutile} = 4.26 g/cm^3 and $\rho_{anatase}$ = 3.84 g/cm^3).

The structural phase of calcined Fe-doped TiO_2 samples is further examined by Raman spectroscopy. Figure 8c reveals the Raman spectra of the produced samples in the 100−700 cm^{-1} range. The Raman spectra of calcined Fe-doped TiO_2 samples are identical with that of calcined pure TiO_2-1.5, which indicates that TiO_2 maintains its structure after Fe doping. However, a closer inspection of Figure 8c (see the inset) reveals a blue-shift and broadening of the sharpest and strongest Eg(1) peak at ∼144 cm^{-1} with increasing iron content in the sample. The intense Eg(1) mode is commonly assigned to vibration in which only Ti moves while oxygen remains stationary.[62] As discussed above, the substitution of Ti^{4+} ions by Fe^{3+} ions would generate oxygen vacancies to maintain the charge equilibrium. Wu et al.[8] found out that the shortening of Ti−O bond length in Fe-doped TiO_2 particles happened as a result of oxygen defect prompted the transformation of coordination geometry from octahedral (TiO_6) in pure TiO_2 to tetrahedral (TiO_4) in Fe-doped TiO_2. Therefore, oxygen vacancies could give rise to a shift in the Raman band toward a higher wavenumber. Furthermore, partial removal and rearrangement of the oxygen ions in TiO_6 octahedral in which Ti ions are surrounded by six O ions to the TiO_{6-n} (n is a number of oxygen vacancies) due to the Fe

https://doi.org/10.1021/acsanm.3c03107
ACS Appl. Nano Mater. 2023, 6, 22660−22672

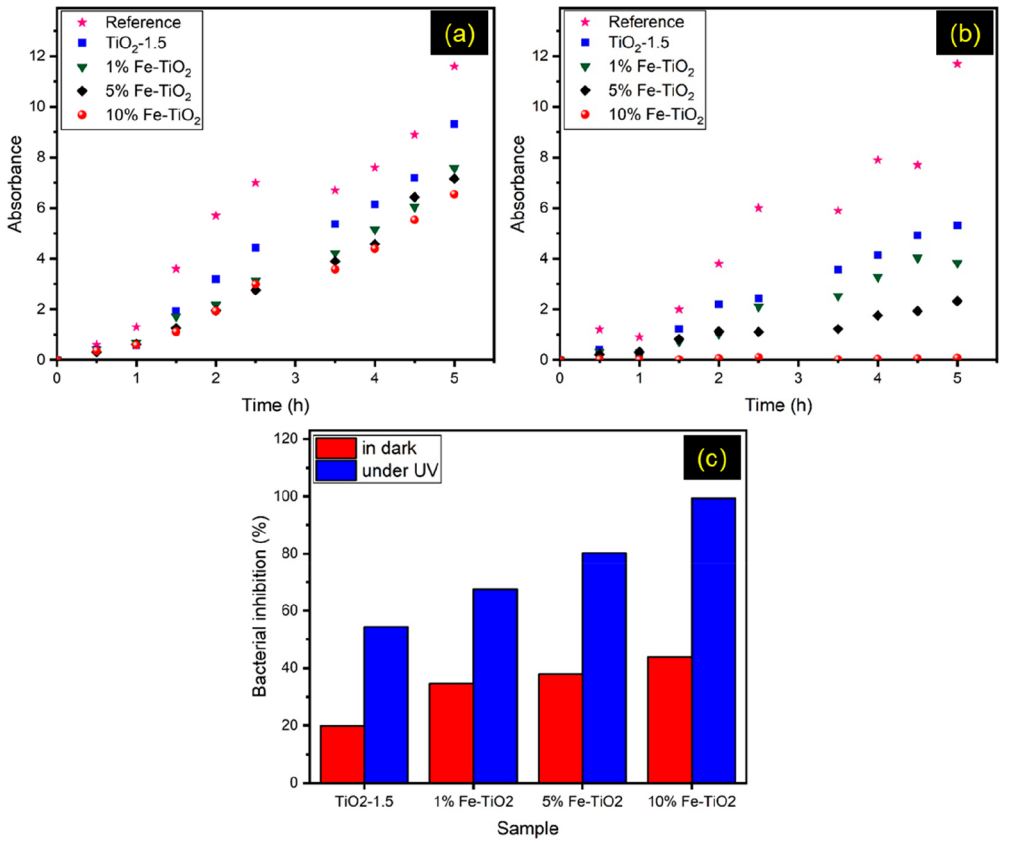

Figure 9. Growth study of spectinomycin-resistant *Escherichia coli* in liquid medium inoculated in the presence of calcined TiO_2-1.5 and Fe-doped TiO_2 samples (0.4 g/L) by studied particles (a) in the dark and (b) under UV (365 nm). (c) Bacterial inhibition percent after cumulative 5 h exposure to UV induced by pure and doped TiO_2 particles in the dark or activated by UV.

doping may result in Raman scattering from the TiO_{6-n} with few Ti−O bonds, resulting in a broad line with low intensity.[62]

Finally, UV−vis spectroscopy measurements were performed to evaluate the role of Fe^{3+} doping in tuning the optical gap energy of samples. Figure S6 shows the optical absorbance spectra for calcined pure TiO_2 and Fe-doped TiO_2 samples. It was observed that calcined Fe-doped TiO_2 samples demonstrate a red-shift of the absorption band, similar to those reported by other investigators.[41,63] The obtained optical gap values (Figure 8d) clearly indicate that the optical gap decreases with increasing Fe concentration in the TiO_2 lattice. According to previous reports, the Fe^{3+} doping into the TiO_2 crystal structure may reduce the optical gap through the creation of a new intermediate energy level (Fe^{3+} t_{2g}) between the conduction and valence band of TiO_2.[64,65] Therefore, the lowering of the optical gap energy after Fe doping should come from the electronic transition from the higher energy state of 3d electrons of Fe dopant to the conduction band of TiO_2.[6] Thus, the incorporation of Fe^{3+} in the TiO_2 lattice may enhance the photoactivity of nanoparticles.

3.3. Fe-Doped TiO_2 Nanoparticles Fighting Bacteria Resistant to Antibiotics. Fe-doped TiO_2 nanoparticles exhibited improved structural and optical properties. These characteristics make Fe-doped TiO_2 nanoparticles promising candidates for applications as antimicrobial agents, particularly against antibiotic-resistant bacteria. In this regard, the growth kinetics of bacteria was monitored in a liquid medium by following the variation in optical density (OD) versus time in the dark (Figure 9a) and under UV light exposure (365 nm; Figure 9b). Note that no impact on the bacteria growth was seen with water or with the physiological solution under the used experimental conditions, neither in the dark nor under UV light.

Figure 9b shows that after UV irradiation bacteria are less activated or even inactivated, which is clearly different compared to the "blank" reference samples. Upon comparison of the calcined Fe-doped TiO_2 with calcined pure TiO_2-1.5 nanoparticles under UV treatment, it becomes evident that the calcined Fe-doped TiO_2 nanoparticles exhibit greater antibiotic activity than that of calcined pure TiO_2-1.5 nanoparticles. In the dark, for spectinomycin-resistant *E. coli* at the end of the bacterial assay, the following OD values were measured: 11.6, 7.6, 7.2, 6.5, and 9.3 for the reference, 1% to 10% Fe−TiO_2, and pure TiO_2-1.5 samples, respectively. The percentage of inhibition was then calculated; this parameter varied from 19.8% to 43.9%. A higher inhibitory effect on the bacteria growth under 365 nm UV light than in the dark was noticed for 1% to 10% Fe−TiO_2 samples, varying from 67.5% to 99.4% (Figure 9c). The findings of our investigation reveal that there exists a positive correlation between the concentration of the Fe dopant in TiO_2 nanoparticles and the inhibitory effect on bacterial growth. It is believed that the enhanced inhibitory effect is related to the formation of oxygen vacancies and a decrease in the optical gap of TiO_2 due to the incorporation of Fe dopants. The oxygen vacancies provide active sites for the adsorption and oxidation of bacteria, while the lowered optical gap increases the absorption of light and promotes the generation of reactive oxygen species (ROS), which can further damage bacterial cells. Thus, the doping of Fe in TiO_2 can serve as an effective strategy to enhance its antibacterial activity and combat antibiotic-resistant bacteria. It is important to note that similar results were

https://doi.org/10.1021/acsanm.3c03107
ACS Appl. Nano Mater. 2023, 6, 22660−22672

obtained with a strain that is not resistant to antibiotics, i.e., *E. coli*. The reported mechanism of action of TiO_2 nanoparticles against the bacteria is related to ROS generation, DNA damage after nanoparticles internalization, peroxidation of membrane phospholipids, and then inhibition of respiration.[66,67] Photoactivation of TiO_2 nanoparticles also remarkably increased its antimicrobial activity as already reported against *E. coli*, *Bacteroides fragilis*, *P. aeruginosa*, *E. hire*, *S. typhimurium*, and *S. aureus*.[68] Under UV light, the presence of iron in the TiO_2 structure increased the antibacterial activity against spectinomycin-resistant *Escherichia coli*.[69,70] The ability of iron to produce free radicals and as discussed before the oxidative stress of TiO_2 increased due to the iron through Fenton reactions all resulting in an enhancement of the antibacterial activity. Overall, our findings suggest that Fe-doped TiO_2 nanoparticles have promising potential as an effective antibacterial agent, particularly when combined with UV light irradiation.

4. CONCLUSIONS

In summary, a facile continuous aerosol-based method was developed to produce pure and Fe-doped TiO_2 nanoparticles by EAFSP. In the EAFSP system, electrostatic forces propel the charged precursor droplets from the electrospray nozzle to the flame. In contrast to conventional FSP, the presented EAFSP synthesis eliminates the requirement for dispersion gas during spraying and avoids the use of complex precursors and solvents with μ-explosion-promoting additives. In this work, pure TiO_2 nanoparticles were prepared initially by electrospraying TDIP at varying concentrations into the flame. In this regard, various *in situ* and *ex situ* process and particle diagnostics such as PDA, high-speed camera, spICP-MS, SMPS, SAXS, TEM, and BET were applied for analyzing in-flight droplet characteristics in the spray as well as primary and agglomerate nanoparticle evolution within the process. TEM and SAXS measurements revealed a bimodal distribution in the primary particles, while spICP-MS provided insights into the particle formation route based on synthesis conditions like precursor concentration. Then, Fe-doped TiO_2 nanoparticles were synthesized by the EAFSP method with Fe/Ti molar ratios of 1, 5, and 10%. It was observed that Fe doping in TiO_2 lattice structure could effectively reduce the crystallite sizes, greatly promote the formation of the rutile phase, spontaneously create oxygen vacancies, and reduce the optical gap energy of TiO_2 nanoparticles. Finally, the antimicrobial activity of the synthesized Fe-doped TiO_2 nanoparticles was evaluated against spectinomycin-resistant *Escherichia coli*, demonstrating a significant inhibitory effect of nanoparticles with an inhibition rate of up to 95% in a liquid medium. These findings suggest the potential of Fe-doped TiO_2 nanoparticles as effective antibacterial agents, particularly under UV light.

■ ASSOCIATED CONTENT

Supporting Information

The Supporting Information is available free of charge at https://pubs.acs.org/doi/10.1021/acsanm.3c03107.

Synthesis of spherical solid TiO_2 nanoparticles for calibration of spICP-MS analysis, details of samples characterization with the high-speed camera, PDA, SMPS, XRD, and SAXS measurements, N_2 adsorption−desorption isotherms of TiO_2 samples, TEM and SEM images of spherical solid TiO_2 nanoparticles produced by spray drying, TEM images of 1% Fe−TiO_2 and 5% Fe−TiO_2 nanoparticles, and UV−vis absorption spectra of pure and doped TiO_2 particles (PDF)

Videos of TDIP-1.5 droplet combustion recorded by a high-speed camera (PPTX)

■ AUTHOR INFORMATION

Corresponding Authors

Jalal Poostforooshan − *Institute of Particle Technology, Clausthal University of Technology, 38678 Clausthal-Zellerfeld, Germany;* orcid.org/0000-0002-8167-5290; Email: jalal.poostforooshan@tu-clausthal.de

Sabrina Belbekhouche − *CNRS, Institut Chimie et Matériaux Paris Est, UMR 7182, Université Paris Est Creteil, 94320 Thiais, France;* orcid.org/0000-0002-0636-4425; Email: belbekhouche@icmpe.cnrs.fr

Authors

Vinzent Olszok − *Institute of Particle Technology, Clausthal University of Technology, 38678 Clausthal-Zellerfeld, Germany;* orcid.org/0000-0003-1961-8268

Malte F. B. Stodt − *Technische Thermodynamik, Universität Bremen, 28359 Bremen, Germany; Leibniz Institute for Materials Engineering IWT, 28359 Bremen, Germany*

Mira Simmler − *Institute of Mechanical Process Engineering and Mechanics, Karlsruhe Institute of Technology, 76131 Karlsruhe, Germany*

Malte Bierwirth − *Institute of Particle Technology, Clausthal University of Technology, 38678 Clausthal-Zellerfeld, Germany*

Hermann Nirschl − *Institute of Mechanical Process Engineering and Mechanics, Karlsruhe Institute of Technology, 76131 Karlsruhe, Germany*

Johannes Kiefer − *Technische Thermodynamik, Universität Bremen, 28359 Bremen, Germany; Leibniz Institute for Materials Engineering IWT, 28359 Bremen, Germany;* orcid.org/0000-0002-0837-3456

Udo Fritsching − *Leibniz Institute for Materials Engineering IWT, 28359 Bremen, Germany; Particles and Process Engineering, University Bremen, 28359 Bremen, Germany;* orcid.org/0000-0003-3167-3657

Alfred P. Weber − *Institute of Particle Technology, Clausthal University of Technology, 38678 Clausthal-Zellerfeld, Germany*

Complete contact information is available at: https://pubs.acs.org/10.1021/acsanm.3c03107

Notes

The authors declare no competing financial interest.

■ ACKNOWLEDGMENTS

The authors gratefully acknowledge the financial support provided by the German Research Foundation (DFG) (under Grants WE 2331/20-1, KI 1396/6-2, FR 912/42-2, Ni 414/30-1, and Ni 414/30-2), as part of the SPP1980 SpraySyn, and the UPEC and CNRS. We appreciate the technical assistance of Dr.-Ing. Gundula Helsch (Institute of Nonmetallic Materials, TU Clausthal) for XRD and Raman characterizations and of Dr. André Pawlak (Institut National de la Santé et de la Recherche Médicale (INSERM), IMRB U955, Créteil, France) for the antibacterial assay.

https://doi.org/10.1021/acsanm.3c03107
ACS Appl. Nano Mater. 2023, 6, 22660−22672

REFERENCES

(1) Roy, P.; Kim, D.; Lee, K.; Spiecker, E.; Schmuki, P. TiO_2 Nanotubes and Their Application in Dye-Sensitized Solar Cells. *Nanoscale* **2010**, *2* (1), 45−59.

(2) Nakata, K.; Fujishima, A. TiO_2 Photocatalysis: Design and Applications. *J. Photochem. Photobiol. C: Photochem. Rev.* **2012**, *13* (3), 169−189.

(3) Tong, T.; Zhang, J.; Tian, B.; Chen, F.; He, D. Preparation of Fe^{3+}-Doped TiO_2 Catalysts by Controlled Hydrolysis of Titanium Alkoxide and Study on Their Photocatalytic Activity for Methyl Orange Degradation. *J. Hazard. Mater.* **2008**, *155* (3), 572−579.

(4) Hoffmann, M. R.; Martin, S. T.; Choi, W.; Bahnemann, D. W. Environmental Applications of Semiconductor Photocatalysis. *Chem. Rev.* **1995**, *95* (1), 69−96.

(5) Choi, W.; Termin, A.; Hoffmann, M. R. The Role of Metal Ion Dopants in Quantum-Sized TiO_2: Correlation between Photoreactivity and Charge Carrier Recombination Dynamics. *J. Phys. Chem.* **1994**, *98* (51), 13669−13679.

(6) Kundu, A.; Mondal, A. Structural, Optical, Physio-Chemical Properties and Photodegradation Study of Methylene Blue Using Pure and Iron-Doped Anatase Titania Nanoparticles under Solar-Light Irradiation. *J. Mater. Sci. Mater. Electron.* **2019**, *30* (4), 3244−3256.

(7) Yamashita, H.; Harada, M.; Misaka, J.; Takeuchi, M.; Neppolian, B.; Anpo, M. Photocatalytic Degradation of Organic Compounds Diluted in Water Using Visible Light-Responsive Metal Ion-Implanted TiO_2 Catalysts: Fe Ion-Implanted TiO_2. *Catal. Today* **2003**, *84* (3), 191−196.

(8) Wu, Q.; Zheng, Q.; van de Krol, R. Creating Oxygen Vacancies as a Novel Strategy To Form Tetrahedrally Coordinated Ti^{4+} in Fe/TiO_2 Nanoparticles. *J. Phys. Chem. C* **2012**, *116* (12), 7219−7226.

(9) Rathore, N.; Kulshreshtha, A.; Shukla, R. K.; Sharma, D. Optical, Structural and Morphological Properties of Fe Substituted Rutile Phase TiO_2 Nanoparticles. *Physica B Condens. Matter* **2021**, *600*, No. 412609.

(10) Nguyen, V. N.; Nguyen, N. K. T.; Nguyen, P. H. Hydrothermal Synthesis of Fe-Doped TiO_2 Nanostructure Photocatalyst. *Adv. Nat. Sci.: Nanosci. Nanotechnol.* **2011**, *2* (3), No. 035014.

(11) Rathore, N.; Shukla, R. K.; Dubey, K. C.; Kulshreshtha, A. Synthesis of Undoped and Fe Doped Nanoparticles of TiO_2 via Co-Precipitation Technique and Their Characterizations. *Mater. Today Proc.* **2020**, *29*, 861−865.

(12) Meierhofer, F.; Fritsching, U. Synthesis of Metal Oxide Nanoparticles in Flame Sprays: Review on Process Technology, Modeling, and Diagnostics. *Energy Fuels* **2021**, *35* (7), 5495−5537.

(13) Bierwirth, M.; Olszok, V.; Ganesan, V. A.; Poostforooshan, J.; Weber, A. P. Analyse Der Partikelbildung Aus Der Elektrospray-Flammensprühpyrolyse Mittels Scanning Mobility Particle Sizer. *Chem. Ing. Technol.* **2021**, *93* (8), 1307−1315.

(14) Geier, M.; Parker, T. Electrospray Flame Synthesis of Yttria-Stabilized Zirconia Nanoparticles. *Ind. Eng. Chem. Res.* **2013**, *52* (47), 16842−16850.

(15) Morais, A. Í. S.; Vieira, E. G.; Afewerki, S.; Sousa, R. B.; Honorio, L. M. C.; Cambrussi, A. N. C. O.; Santos, J. A.; Bezerra, R. D. S.; Furtini, J. A. O.; Silva-Filho, E. C.; Webster, T. J.; Lobo, A. O. Fabrication of Polymeric Microparticles by Electrospray: The Impact of Experimental Parameters. *J. Funct. Biomater.* **2020**, *11* (1), 4.

(16) Anderson, A.-L.; Binions, R. The Effect of Brij® Surfactants in Sol−Gel Processing for the Production of TiO_2 Thin Films. *Polyhedron* **2015**, *85*, 83−92.

(17) Cho, Y.; Lee, Y.; Ku, N.; Ji, S.; Kim, Y. Synthesis of Porous Particles by Electrospray-Assisted Self-Assembly for Water-Repellent or Photocatalytic Surfaces. *Korean J. Met. Mater.* **2020**, *58* (2), 112−124.

(18) Gold, K.; Slay, B.; Knackstedt, M.; Gaharwar, A. K. Antimicrobial Activity of Metal and Metal-Oxide Based Nanoparticles. *Adv. Ther.* **2018**, *1* (3), No. 1700033.

(19) Pinto-Alphandary, H.; Andremont, A.; Couvreur, P. Targeted Delivery of Antibiotics Using Liposomes and Nanoparticles: Research and Applications. *Int. J. Antimicrob. Agents* **2000**, *13* (3), 155−168.

(20) Ali Said, F.; Bousserrhine, N.; Alphonse, V.; Michely, L.; Belbekhouche, S. Antibiotic Loading and Development of Antibacterial Capsules by Using Porous $CaCO_3$ Microparticles as Starting Material. *Int. J. Pharm.* **2020**, *579*, No. 119175.

(21) Mislin, G. L. A.; Schalk, I. J. Siderophore-Dependent Iron Uptake Systems as Gates for Antibiotic Trojan Horse Strategies against Pseudomonas Aeruginosa. *Metallomics* **2014**, *6* (3), 408−420.

(22) Poostforooshan, J.; Belbekhouche, S.; Shaban, M.; Alphonse, V.; Habert, D.; Bousserrhine, N.; Courty, J.; Weber, A. Aerosol-Assisted Synthesis of Tailor-Made Hollow Mesoporous Silica Microspheres for Controlled Release of Antibacterial and Anticancer Agents. *ACS Appl. Mater. Interfaces* **2020**, *12* (6), 6885−6898.

(23) Belbekhouche, S.; Poostforooshan, J.; Shaban, M.; Ferrara, B.; Alphonse, V.; Cascone, I.; Bousserrhine, N.; Courty, J.; Weber, A. P. Fabrication of Large Pore Mesoporous Silica Microspheres by Salt-Assisted Spray-Drying Method for Enhanced Antibacterial Activity and Pancreatic Cancer Treatment. *Int. J. Pharm.* **2020**, *590*, No. 119930.

(24) Pelgrift, R. Y.; Friedman, A. J. Nanotechnology as a Therapeutic Tool to Combat Microbial Resistance. *Adv. Drug Delivery Rev.* **2013**, *65* (13), 1803−1815.

(25) Akbari, V.; Abedi, D.; Pardakhty, A.; Sadeghi-Aliabadi, H. Ciprofloxacin Nano-Niosomes for Targeting Intracellular Infections: An in Vitro Evaluation. *J. Nanoparticle Res.* **2013**, *15* (4), 1556.

(26) Xi, A.; Bothun, G. D. Centrifugation-Based Assay for Examining Nanoparticle−Lipid Membrane Binding and Disruption. *Analyst* **2014**, *139* (5), 973−981.

(27) von Moos, N.; Slaveykova, V. I. Oxidative Stress Induced by Inorganic Nanoparticles in Bacteria and Aquatic Microalgae − State of the Art and Knowledge Gaps. *Nanotoxicology* **2014**, *8* (6), 605−630.

(28) Ahmad, J.; Dwivedi, S.; Alarifi, S.; Al-Khedhairy, A. A.; Musarrat, J. Use of β-Galactosidase (LacZ) Gene α-Complementation as a Novel Approach for Assessment of Titanium Oxide Nanoparticles Induced Mutagenesis. *Mutat. Res. - Genet. Toxicol. Environ. Mutagen.* **2012**, *747* (2), 246−252.

(29) Li, K.; Zhao, X.; Hammer, B. K.; Du, S.; Chen, Y. Nanoparticles Inhibit DNA Replication by Binding to DNA: Modeling and Experimental Validation. *ACS Nano* **2013**, *7* (11), 9664−9674.

(30) Choi, O.; Deng, K. K.; Kim, N.-J.; Ross, L.; Surampalli, R. Y.; Hu, Z. The Inhibitory Effects of Silver Nanoparticles, Silver Ions, and Silver Chloride Colloids on Microbial Growth. *Water Res.* **2008**, *42* (12), 3066−3074.

(31) Olin, S. S. The Relevance of the Rat Lung Response to Particle Overload for Human Risk Assessment: A Workshop Consensus Report. *Inhal. Toxicol.* **2000**, *12* (1−2), 1−17.

(32) Zhao, J.; Bowman, L.; Zhang, X.; Vallyathan, V.; Young, S.-H.; Castranova, V.; Ding, M. Titanium Dioxide (TiO_2) Nanoparticles Induce JB6 Cell Apoptosis Through Activation of the Caspase-8/Bid and Mitochondrial Pathways. *J. Toxicol. Environ. Health A* **2009**, *72* (19), 1141−1149.

(33) Boucher, H. W.; Talbot, G. H.; Bradley, J. S.; Edwards, J. E.; Gilbert, D.; Rice, L. B.; Scheld, M.; Spellberg, B.; Bartlett, J. Bad Bugs, No Drugs: No ESKAPE! An Update from the Infectious Diseases Society of America. *Clin. Infect. Dis.* **2009**, *48* (1), 1−12.

(34) Pendleton, J. N.; Gorman, S. P.; Gilmore, B. F. Clinical Relevance of the ESKAPE Pathogens. *Expert Rev. Anti-Infect. Ther.* **2013**, *11* (3), 297−308.

(35) Hegreness, M.; Shoresh, N.; Damian, D.; Hartl, D.; Kishony, R. Accelerated Evolution of Resistance in Multidrug Environments. *Proc. Natl. Acad. Sci. U. S. A.* **2008**, *105* (37), 13977−13981.

(36) Wolska, K.; Grzes, K. M.; Kurek, A. Synergy between Novel Antimicrobials and Conventional Antibiotics or Bacteriocins. *Polym. J. Microbiol.* **2012**, *61* (2), 95−104.

(37) Vakulenko, S. B.; Mobashery, S. Versatility of Aminoglycosides and Prospects for Their Future. *Clin. Microbiol. Rev.* **2003**, *16* (3), 430−450.

(38) Kehrenberg, C.; Catry, B.; Haesebrouck, F.; de Kruif, A.; Schwarz, S. Novel Spectinomycin/Streptomycin Resistance Gene, *AadA14*, from *Pasteurella Multocida*. *Antimicrob. Agents Chemother.* **2005**, *49* (7), 3046−3049.

(39) Mohammadi, S.; Poostforooshan, J.; Stodt, M. F. B.; Olszok, V.; Kiefer, J.; Fritsching, U.; Weber, A. P. Tailoring Crystal Structure and

https://doi.org/10.1021/acsanm.3c03107
ACS Appl. Nano Mater. 2023, 6, 22660−22672

Morphology of MnO_x Nanoparticles via Electrospray-Assisted Flame Spray Pyrolysis. *Appl. Energy Combust. Sci.* **2023**, *14*, No. 100151.
(40) Martins, F. J. W. A.; Kirchmann, J.; Kronenburg, A.; Beyrau, F. Experimental Investigation of Axisymmetric, Turbulent, Annular Jets Discharged through the Nozzle of the SPP1980 SpraySyn Burner under Isothermal and Reacting Conditions. *Exp. Therm. Fluid Sci.* **2020**, *114*, No. 110052.
(41) Shyniya, C. R.; Bhabu, K. A.; Rajasekaran, T. R. Enhanced Electrochemical Behavior of Novel Acceptor Doped Titanium Dioxide Catalysts for Photocatalytic Applications. *J. Mater. Sci. Mater. Electron.* **2017**, *28* (9), 6959−6970.
(42) Abram, C.; Mezhericher, M.; Beyrau, F.; Stone, H. A.; Ju, Y. Flame Synthesis of Nanophosphors Using Sub-Micron Aerosols. *Proc. Combust. Inst.* **2019**, *37* (1), 1231−1239.
(43) Pokhrel, S.; Mädler, L. Flame-Made Particles for Sensors, Catalysis, and Energy Storage Applications. *Energy Fuels* **2020**, *34* (11), 13209−13224.
(44) Li, H.; Pokhrel, S.; Schowalter, M.; Rosenauer, A.; Kiefer, J.; Mädler, L. The Gas-Phase Formation of Tin Dioxide Nanoparticles in Single Droplet Combustion and Flame Spray Pyrolysis. *Combust. Flame* **2020**, *215*, 389−400.
(45) Rosebrock, C. D.; Wriedt, T.; Mädler, L.; Wegner, K. The Role of Microexplosions in Flame Spray Synthesis for Homogeneous Nanopowders from Low-Cost Metal Precursors. *AIChE J.* **2016**, *62* (2), 381−391.
(46) Stodt, M. F. B.; Groeneveld, J. D.; Mädler, L.; Kiefer, J.; Fritsching, U. Microexplosions of Multicomponent Drops in Spray Flames. *Combust. Flame* **2022**, *240*, No. 112043.
(47) Stodt, M. F. B.; Kiefer, J.; Fritsching, U. Impact of Atomization and Spray Flow Conditions on Droplet μ-Explosions and Temporal Self-Similarity in the FSP Process. *Appl. Energy Combust. Sci.* **2023**, *15*, No. 100170.
(48) Gröhn, A. J.; Pratsinis, S. E.; Sánchez-Ferrer, A.; Mezzenga, R.; Wegner, K. Scale-up of Nanoparticle Synthesis by Flame Spray Pyrolysis: The High-Temperature Particle Residence Time. *Ind. Eng. Chem. Res.* **2014**, *53* (26), 10734−10742.
(49) Wu, C.; Zhang, Y.; Yang, L.; Xiao, B.; Jiao, A.; Li, K.; Chen, T.; Huang, Z.; Lin, H. Flame Spray Pyrolysis Synthesis of WO_3 Sensing Materials: Effects of Flame Parameters on Particle Size Distribution and NO_2 Sensing Performance. *Langmuir* **2022**, *38* (50), 15506−15515.
(50) Bierwirth, M.; Olszok, V.; Wollmann, A.; Weber, A. P. A New Coupling Setup of DMA, CPC and Sp-ICP-MS with Increased Versatility. *J. Aerosol Sci.* **2022**, *163*, No. 105983.
(51) Li, H.; Rosebrock, C. D.; Wu, Y.; Wriedt, T.; Mädler, L. Single Droplet Combustion of Precursor/Solvent Solutions for Nanoparticle Production: Optical Diagnostics on Single Isolated Burning Droplets with Micro-Explosions. *Proc. Combust. Inst.* **2019**, *37* (1), 1203−1211.
(52) Gonchikzhapov, M.; Kasper, T. Decomposition Reactions of $Fe(CO)_5$, $Fe(C_5H_5)_2$, and TTIP as Precursors for the Spray-Flame Synthesis of Nanoparticles in Partial Spray Evaporation at Low Temperatures. *Ind. Eng. Chem. Res.* **2020**, *59* (18), 8551−8561.
(53) Sorensen, C. M. Light Scattering by Fractal Aggregates: A Review. *Aerosol Sci. Technol.* **2001**, *35* (2), 648−687.
(54) Meakin, P. Formation of Fractal Clusters and Networks by Irreversible Diffusion-Limited Aggregation. *Phys. Rev. Lett.* **1983**, *51* (13), 1119−1122.
(55) Calisir, M. D.; Gungor, M.; Demir, A.; Kilic, A.; Khan, M. M. Nitrogen-Doped TiO_2 Fibers for Visible-Light-Induced Photocatalytic Activities. *Ceram. Int.* **2020**, *46* (10), 16743−16753.
(56) He, H.; Sun, D.; Zhang, Q.; Fu, F.; Tang, Y.; Guo, J.; Shao, M.; Wang, H. Iron-Doped Cauliflower-Like Rutile TiO_2 with Superior Sodium Storage Properties. *ACS Appl. Mater. Interfaces* **2017**, *9* (7), 6093−6103.
(57) Jamalluddin, N. A.; Abdullah, A. Z. Reactive Dye Degradation by Combined Fe(III)/TiO_2 Catalyst and Ultrasonic Irradiation: Effect of Fe(III) Loading and Calcination Temperature. *Ultrason. Sonochem.* **2011**, *18* (2), 669−678.
(58) Ismail, M. A.; Hedhili, M. N.; Anjum, D. H.; Singaravelu, V.; Chung, S. H. Synthesis and Characterization of Iron-Doped TiO_2 Nanoparticles Using Ferrocene from Flame Spray Pyrolysis. *Catalysts* **2021**, *11* (4), 438.
(59) Soria, J.; Conesa, J. C.; Augugliaro, V.; Palmisano, L.; Schiavello, M.; Sclafani, A. Dinitrogen Photoreduction to Ammonia over Titanium Dioxide Powders Doped with Ferric Ions. *J. Phys. Chem.* **1991**, *95* (1), 274−282.
(60) Wang, X. H.; Li, J.-G.; Kamiyama, H.; Katada, M.; Ohashi, N.; Moriyoshi, Y.; Ishigaki, T. Pyrogenic Iron(III)-Doped TiO_2 Nanopowders Synthesized in RF Thermal Plasma: Phase Formation, Defect Structure, Band Gap, and Magnetic Properties. *J. Am. Chem. Soc.* **2005**, *127* (31), 10982−10990.
(61) Wang, Z.-M.; Yang, G.; Biswas, P.; Bresser, W.; Boolchand, P. Processing of Iron-Doped Titania Powders in Flame Aerosol Reactors. *Powder Technol.* **2001**, *114* (1), 197−204.
(62) Choudhury, B.; Verma, R.; Choudhury, A. Oxygen Defect Assisted Paramagnetic to Ferromagnetic Conversion in Fe Doped TiO_2 Nanoparticles. *RSC Adv.* **2014**, *4* (55), 29314−29323.
(63) Teoh, W. Y.; Amal, R.; Mädler, L.; Pratsinis, S. E. Flame Sprayed Visible Light-Active Fe-TiO_2 for Photomineralisation of Oxalic Acid. *Catal. Today* **2007**, *120* (2), 203−213.
(64) Zhang, J.; Chen, X.; Shen, Y.; Li, Y.; Hu, Z.; Chu, J. Synthesis, Surface Morphology, and Photoluminescence Properties of Anatase Iron-Doped Titanium Dioxide Nano-Crystalline Films. *Phys. Chem. Chem. Phys.* **2011**, *13* (28), 13096−13105.
(65) Rathore, N.; Kulshreshtha, A.; Shukla, R. K.; Sharma, D. Optical, Structural and Morphological Properties of Fe Substituted Rutile Phase TiO_2 Nanoparticles. *Phys. Rev. B Condens. Matter* **2021**, *600*, No. 412609.
(66) Kumar, A.; Pandey, A. K.; Singh, S. S.; Shanker, R.; Dhawan, A. Engineered ZnO and TiO_2 Nanoparticles Induce Oxidative Stress and DNA Damage Leading to Reduced Viability of Escherichia Coli. *Free Radic. Biol. Med.* **2011**, *51* (10), 1872−1881.
(67) Tsuang, Y.-H.; Sun, J.-S.; Huang, Y.-C.; Lu, C.-H.; Chang, W. H.-S.; Wang, C.-C. Studies of Photokilling of Bacteria Using Titanium Dioxide Nanoparticles. *Artif. Organs* **2008**, *32* (2), 167−174.
(68) Maness, P.-C.; Smolinski, S.; Blake, D. M.; Huang, Z.; Wolfrum, E. J.; Jacoby, W. A. Bactericidal Activity of Photocatalytic TiO_2 Reaction: Toward an Understanding of Its Killing Mechanism. *Appl. Environ. Microbiol.* **1999**, *65* (9), 4094−4098.
(69) Arellano, U.; Asomoza, M.; Ramírez, F. Antimicrobial Activity of Fe−TiO_2 Thin Film Photocatalysts. *J. Photochem. Photobiol. A. Chem.* **2011**, *222* (1), 159−165.
(70) Sonawane, R. S.; Kale, B. B.; Dongare, M. K. Preparation and Photo-Catalytic Activity of Fe TiO_2 Thin Films Prepared by Sol−Gel Dip Coating. *Mater. Chem. Phys.* **2004**, *85* (1), 52−57.

https://doi.org/10.1021/acsanm.3c03107
ACS Appl. Nano Mater. 2023, 6, 22660−22672